

Energy Dissipation Preserving Feature-based DNN Galerkin Methods for Gradient Flows

Tao Tang^{d,g}, Jiang Yang^{a,c,e,f,*}, Yuxiang Zhao^a, Quanhui Zhu^b

^a*Department of Mathematics, Southern University of Science and Technology, Shenzhen, China.*

^b*Department of Mathematics, National University of Singapore, Singapore.*

^c*SUSTech International Center for Mathematics, Shenzhen, China.*

^d*School of Mathematics and Statistics, Guangzhou Nanfang College, Guangzhou, China.*

^e*Guangdong Provincial Key Laboratory of Computational Science and Material Design, SUSTech, Shenzhen, China.*

^f*National Center for Applied Mathematics Shenzhen (NCAMS), Shenzhen, China.*

^g*Zhuhai SimArk Technology Co., LTD, Zhuhai, China.*

Abstract

In recent years, deep learning methods, exemplified by Physics-Informed Neural Networks (PINNs), have been widely applied to the numerical solution of differential equations. However, these methods may suffer from limited accuracy, high training costs, and lack of robustness, particularly their inability to preserve the intrinsic physical structures of continuous PDE models, such as the energy dissipation property in gradient flow systems. To address these challenges, we propose a feature-based Deep Neural Network Galerkin (DNN-G) framework designed for structure-preserving simulations of gradient flows. Instead of treating neural networks merely as optimization-driven solvers, we employ them as adaptive feature generators that define nonlinear trial spaces within a Galerkin projection formulation. This formulation guarantees semi-discrete energy dissipation and can be naturally combined with energy stable time integration schemes. Several strategies for constructing neural basis functions are investigated, including random features, structured initialization, and problem-informed pre-training. Numerical experiments demonstrate that the proposed method preserves robust energy stability in

*Corresponding author.

Email addresses: ttang@nfsu.edu.cn (T. Tang), yangj7@sustech.edu.cn (J. Yang), 12131241@mail.sustech.edu.cn (Y. Zhao), zhuqh@nus.edu.sg (Q. Zhu)

high-dimensional settings and accurately captures complex topological transitions. With equivalent degrees of freedom, the DNN-G framework achieves higher accuracy than classical spectral methods, highlighting the effectiveness of neural feature representations for the numerical solution of partial differential equations.

Keywords: Deep learning, Gradient flows, Energy dissipation, Galerkin methods

1. Introduction

The numerical simulation of gradient flows plays a fundamental role in material science, fluid mechanics, and biological modeling. A broad class of dissipative systems can be formulated in the form

$$\frac{\partial u}{\partial t} = \mathcal{G} \frac{\delta E}{\delta u}, \quad x \in \Omega, \quad t \in [0, T], \quad (1)$$

where $E[u]$ is an energy functional and \mathcal{G} is a negative semi-definite operator characterizing the dissipation mechanism. This formulation immediately implies the energy dissipation law

$$\frac{dE}{dt} = \int_{\Omega} \frac{\delta E}{\delta u} \cdot \mathcal{G} \frac{\delta E}{\delta u} dx \leq 0, \quad (2)$$

which governs the long-time dynamics of the system. Preserving this structure at the discrete level is therefore essential for physical fidelity and numerical stability.

Over the past decades, extensive efforts in numerical analysis have led to a variety of energy-stable schemes, including convex splitting methods [1, 2], scalar auxiliary variable approaches [3, 4], invariant energy quadratization methods [5], stabilized implicit-explicit schemes [6, 7], and exponential time differencing methods [8, 9, 10, 11, 12]. These methods provide rigorous energy stability and high-order temporal accuracy. Nevertheless, most of them rely on mesh-based discretizations and their efficiency may deteriorate in high-dimensional problems or in situations involving complex geometries and topological changes.

Recently, deep neural networks (DNNs) have emerged as a flexible mesh-free framework for solving partial differential equations. Representative approaches include Physics-Informed Neural Networks (PINNs) [13] and related

neural PDE solvers [14, 15, 16, 17], that approximate the solution or the solution operator using a neural network. Their expressive power and mesh-free nature make them attractive for high-dimensional problems and complex geometries [18, 19, 20, 21, 22]. Extensions to gradient flow problems have also been explored [23, 24, 25].

Despite their flexibility, ensuring physical consistency in neural PDE solvers remains a significant challenge. Most existing approaches enforce the governing equations through penalty terms in a loss function, leading to a soft-constraint formulation [26]. For dissipative systems such as gradient flows, this strategy generally does not guarantee the discrete energy dissipation law. As a consequence, numerical solutions may exhibit artificial energy growth or oscillations, particularly in stiff regimes or long-time simulations. Developing neural solvers that rigorously preserve the intrinsic variational structure therefore remains an open problem.

Recent efforts to bridge this gap have explored diverse strategies. Hu et al. [27] proposed an energetic variational neural network in which the energy functional is directly embedded into a time-stepping optimization procedure. Zhang et al. [28] combined operator learning with the SAV methodology to ensure the dissipation of a modified energy functional. While promising, these approaches typically rely on optimization at each time step or specialized network architectures. A general framework that combines neural representations with structure-preserving numerical discretizations remains largely unexplored.

To address these challenges, we propose a structure-preserving deep neural network Galerkin (DNN-G) framework for gradient flows. Instead of treating neural networks as optimization-based solvers, we interpret the outputs of the last hidden layer as adaptive basis functions that define a nonlinear trial space. By projecting the gradient flow equation onto this neural trial space, we obtain a semi-discrete dynamical system for the coefficients. We show that this projected system inherits the energy dissipation law of the original continuous problem, thereby providing a rigorous structure-preserving guarantee at the semi-discrete level.

The main contributions of this work are summarized as follows:

- **Structure-preserving DNN-Galerkin formulation.** We establish a Galerkin projection framework based on neural basis functions that guarantees semi-discrete energy dissipation for gradient flows. The resulting semi-discrete system can be combined naturally with high-order

time integration schemes.

- **Adaptive neural basis construction.** We propose strategies for constructing and updating neural trial spaces during the evolution process. The adaptive mechanism allows the basis functions to track sharp interfaces, multiscale coarsening dynamics, and topological changes.
- **Scalability and high-order accuracy.** Numerical experiments demonstrate that the proposed method achieves higher accuracy under the same degrees of freedom compared with classical spectral discretizations, while maintaining high-order temporal accuracy and good scalability in higher-dimensional problems.

The remainder of this paper is organized as follows. Section 2 presents the theoretical formulation of the DNN-Galerkin method and establishes its energy-dissipative property. Section 3 discusses the construction and adaptation of neural basis functions. Section 4 provides numerical experiments demonstrating accuracy, stability, and scalability. Conclusions are drawn in Section 5.

2. Structure-Preserving DNN Galerkin Scheme

In this section, we develop a structure-preserving numerical framework for gradient flows based on neural Galerkin discretization. Instead of treating neural networks as direct solvers for the PDE, we interpret the outputs of the last hidden layer as adaptive basis functions that define a nonlinear trial space. Projecting the gradient flow equation onto this neural trial space yields a semi-discrete dynamical system for the coefficients. Unlike residual-minimization approaches such as Physics-Informed Neural Networks or Deep Galerkin Methods, the resulting formulation naturally preserves the energy dissipation structure of the underlying variational problem.

2.1. Neural basis functions

We employ a standard feedforward neural network to generate parameterized basis functions:

$$\begin{aligned} z_0 &= I(x), \\ z_l &= \sigma(W_l z_{l-1} + b_l), \quad l = 1, \dots, L, \end{aligned} \tag{3}$$

where $I(x)$ denotes the input feature mapping, W_l and b_l are weight matrices and bias vectors, and σ is the activation function. Let

$$\Phi(x; \theta) = \{\phi_1(x; \theta), \dots, \phi_m(x; \theta)\} = z_L \quad (4)$$

denote the vector of neural features extracted from the last hidden layer [29] where $\theta = \{W_l, b_l\}_{l=1}^L$ collects all trainable parameters.

When the parameter θ is fixed, $\Phi(x; \theta)$ defines a finite-dimensional trial space

$$\mathcal{V}_\theta = \text{span}\{\phi_1(x; \theta), \dots, \phi_m(x; \theta)\}. \quad (5)$$

The trial space is generally nonlinear in the parameter θ but linear in the coefficients $\beta(t)$, which allows the projected system to retain a linear mass matrix structure.

To incorporate the initial condition exactly, we augment the basis by including

$$\phi_0(x) = u_0(x), \quad \phi_{m+1}(x) = 1, \quad (6)$$

and define the augmented basis

$$\Phi_a(x; \theta) = [u_0(x), \phi_1(x; \theta), \dots, \phi_m(x; \theta), 1]^T. \quad (7)$$

The semi-discrete solution is represented as

$$u_h(x, t) = \sum_{i=0}^{m+1} \beta_i(t) \phi_i(x; \theta) = \beta(t)^T \Phi_a(x; \theta), \quad (8)$$

where $\beta(t) \in \mathbb{R}^{m+2}$ are time-dependent coefficients. Choosing $\beta(0) = [1, 0, \dots, 0]^T$ ensures $u_h(x, 0) = u_0(x)$ exactly.

For periodic domains Ω with period L , periodicity is enforced through an input feature embedding

$$I(x) = \left(\cos\left(\frac{2\pi x}{L}\right), \sin\left(\frac{2\pi x}{L}\right) \right), \quad (9)$$

so that all neural basis functions are periodic by construction.

2.2. Semi-discrete DNN-Galerkin System

To facilitate the analysis of the energy dissipation property, we introduce the auxiliary variable v and the gradient flow (1) can then be written in the mixed form

$$\begin{cases} \frac{\partial u}{\partial t} = \mathcal{G}v, \\ v = \frac{\delta E}{\delta u}. \end{cases} \quad (10)$$

We approximate both u and v in the neural trial space \mathcal{V}_θ . The semi-discrete solution for u and v is given by

$$u_h(x, t) = \sum_{i=0}^{m+1} \beta_i(t) \phi_i(x; \theta), \quad v_h(x, t) = \sum_{i=0}^{m+1} \gamma_i(t) \phi_i(x; \theta). \quad (11)$$

The mixed Galerkin formulation reads: Find $u_h, v_h \in \mathcal{V}_\theta$ such that

$$\begin{aligned} \int_{\Omega} \partial_t u_h \psi dx &= \int_{\Omega} \mathcal{G} v_h \psi dx, \quad \forall \psi \in \mathcal{V}_\theta, \\ \int_{\Omega} v_h \psi dx &= \int_{\Omega} \frac{\delta E}{\delta u}(u_h) \psi dx, \quad \forall \psi \in \mathcal{V}_\theta. \end{aligned} \quad (12)$$

Substituting the neural expansions leads to the finite-dimensional system

$$\begin{aligned} \mathbf{M}(\theta) \dot{\beta} &= \mathbf{G}(\theta) \gamma, \\ \mathbf{M}(\theta) \gamma &= \mathbf{r}(\beta), \end{aligned} \quad (13)$$

where

$$M_{ij} = \int_{\Omega} \phi_i \phi_j dx, \quad G_{ij} = \int_{\Omega} \phi_i \mathcal{G} \phi_j dx, \quad r_i(\beta) = \int_{\Omega} \frac{\delta E}{\delta u}(u_h) \phi_i dx. \quad (14)$$

Since $\mathbf{M}(\theta)$ is symmetric positive definite whenever the neural basis functions are linearly independent, the above system defines a finite-dimensional dynamical system.

2.3. Energy Dissipation Preservation

We show that the mixed neural Galerkin system inherits the intrinsic energy dissipation property of the continuous gradient flow.

Theorem 1. *Assume that the operator \mathcal{G} is symmetric negative semi-definite and that the neural basis functions are linearly independent so that the mass matrix $\mathbf{M}(\theta)$ is symmetric positive definite. Then the semi-discrete solution satisfies*

$$\frac{d}{dt}E[u_h(t)] \leq 0. \quad (15)$$

Proof. Define the discrete energy

$$\mathcal{E}(t) = E[u_h(\cdot, t)]. \quad (16)$$

By the chain rule and the definition of the variational derivative, we have

$$\frac{d}{dt}\mathcal{E}(t) = \int_{\Omega} \frac{\delta E}{\delta u}(u_h) \partial_t u_h dx. \quad (17)$$

From the second equation of the mixed formulation, we have

$$\int_{\Omega} v_h \psi dx = \int_{\Omega} \frac{\delta E}{\delta u}(u_h) \psi dx, \quad \forall \psi \in \mathcal{V}_{\theta}. \quad (18)$$

Since the neural basis functions are time-independent, we have $\partial_t u_h \in \mathcal{V}_{\theta}$. Choosing $\psi = \partial_t u_h$ yields

$$\frac{d}{dt}\mathcal{E}(t) = \int_{\Omega} v_h \partial_t u_h dx. \quad (19)$$

Using the first equation of Eq. (12) and choosing $\psi = v_h$, we obtain

$$\int_{\Omega} v_h \partial_t u_h dx = \int_{\Omega} v_h (\mathcal{G}v_h) dx. \quad (20)$$

Since \mathcal{G} is symmetric negative semidefinite,

$$\int_{\Omega} v_h (\mathcal{G}v_h) dx \leq 0, \quad (21)$$

which immediately implies

$$\frac{d}{dt}E[u_h(t)] = \int_{\Omega} v_h (\mathcal{G}v_h) dx \leq 0. \quad (22)$$

□

Theorem 1 establishes that the proposed DNN-Galerkin formulation preserves the energy dissipation property at the semi-discrete level. In practical computations, the resulting ODE system must be further discretized in time. To illustrate how the dissipation structure can be preserved at the fully discrete level, we present a representative example for the L^2 gradient flow.

Example 1 (Fully discrete energy-stable scheme for L^2 gradient flow). Consider the L^2 gradient flow, where the metric operator reduces to the negative identity, $\mathcal{G} = -I$. In this case the operator matrix becomes $\mathbf{G}(\theta) = -\mathbf{M}(\theta)$, and the semi-discrete system (13) reduces to

$$\mathbf{M}(\theta)\dot{\beta} = -\nabla_{\beta}\mathcal{E}(\beta). \quad (23)$$

For a typical Ginzburg–Landau free energy functional

$$E[u] = \int_{\Omega} \left(\frac{\epsilon^2}{2} |\nabla u|^2 + F(u) \right) dx, \quad (24)$$

the gradient of the discrete energy can be evaluated via integration by parts, yielding a decomposition:

$$\mathbf{M}(\theta)\dot{\beta} = -\epsilon^2\mathbf{K}\beta - \mathbf{g}(\beta), \quad (25)$$

where

$$K_{ij} = \int_{\Omega} \nabla\phi_i \cdot \nabla\phi_j dx, \quad g_i(\beta) = \int_{\Omega} F'(u_h)\phi_i dx. \quad (26)$$

To integrate this semi-discrete system while preserving the dissipative structure, we adopt the energy-stabilized two-stage IMEX scheme proposed in [7]. Artificial stabilization parameters $\alpha \geq 0$ and $S \geq 0$ are introduced to guarantee unconditional energy dissipation. The diffusion term is treated implicitly, while the nonlinear term is handled explicitly.

The fully discrete IMEX-RK2 scheme is given as follows:

$$\begin{aligned} \text{Stage 1:} \quad \mathbf{M} \frac{\beta^* - \beta^n}{\gamma\Delta t} &= -\epsilon^2\mathbf{K}\beta^* - \mathbf{g}(\beta^n) \\ &\quad - \alpha\epsilon^2\mathbf{K}(\beta^* - \beta^n) - S\mathbf{M}(\beta^* - \beta^n), \\ \text{Stage 2:} \quad \mathbf{M} \frac{\beta^{n+1} - \beta^n}{\Delta t} &= -\epsilon^2\mathbf{K}[(1-\gamma)\beta^* + \gamma\beta^{n+1}] \\ &\quad - [\delta\mathbf{g}(\beta^n) + (1-\delta)\mathbf{g}(\beta^*)] \\ &\quad - \alpha\epsilon^2\mathbf{K}[\gamma(\beta^{n+1} - \beta^*) + \delta(\beta^* - \beta^n)] \\ &\quad - S\mathbf{M}[\gamma(\beta^{n+1} - \beta^*) + \delta(\beta^* - \beta^n)]. \end{aligned} \quad (27)$$

Here $\gamma = 1 - 1/\sqrt{2}$ and $\delta = 1 - 1/(2\gamma)$. The resulting fully discrete DNN-Galerkin scheme is second-order accurate in time and unconditionally energy stable. The detailed proof of the discrete energy law can be found in [7] and is therefore omitted here.

This example demonstrates that the semi-discrete DNN-Galerkin formulation can be naturally combined with existing structure-preserving time integrators to construct fully discrete schemes that retain the energy dissipation property.

Remark 1. The semi-discrete system (13) can be written as

$$\frac{d\beta}{dt} = \mathbf{M}^{-1}\mathbf{G}\mathbf{M}^{-1}\mathbf{r}(\beta). \quad (28)$$

Although the energy dissipation property is independent of the specific neural network architecture and holds for any linearly independent neural basis, the conditioning of \mathbf{M} strongly affects numerical stability in practice. Nearly linearly dependent basis functions may lead to an ill-conditioned system, motivating the adaptive basis construction introduced in the next section.

3. Choice of Neural Basis Functions

While Theorem 2.1 guarantees unconditional semi-discrete energy stability, the overall accuracy and robustness of the method are primarily determined by the quality of the neural trial space. Unlike traditional discretizations where basis functions are fixed (e.g., Fourier modes or finite elements), the DNN Galerkin framework allows the trial space \mathcal{V}_θ to be generated and adapted through neural features. Consequently, the construction of neural basis functions becomes a central component of the proposed methodology. This section presents a strategy for constructing and refining the neural basis, including two approaches illustrated in Figure 1:

- **Randomized Basis Construction.** A static neural basis is first generated under the Random Features paradigm, providing universal approximation without iterative training. On this foundation, a structured first-layer initialization (SFLI) is introduced to enhance linear independence and improve the spectral properties of the mass matrix.

- Problem-Informed Basis Refinement.** Starting from the structured static basis $\Phi(x, t; \theta_0)$, equation-specific information is incorporated either through initial-condition alignment or through residual-driven pre-training. This produces either a frozen problem-adapted basis or a time-local adaptive basis.

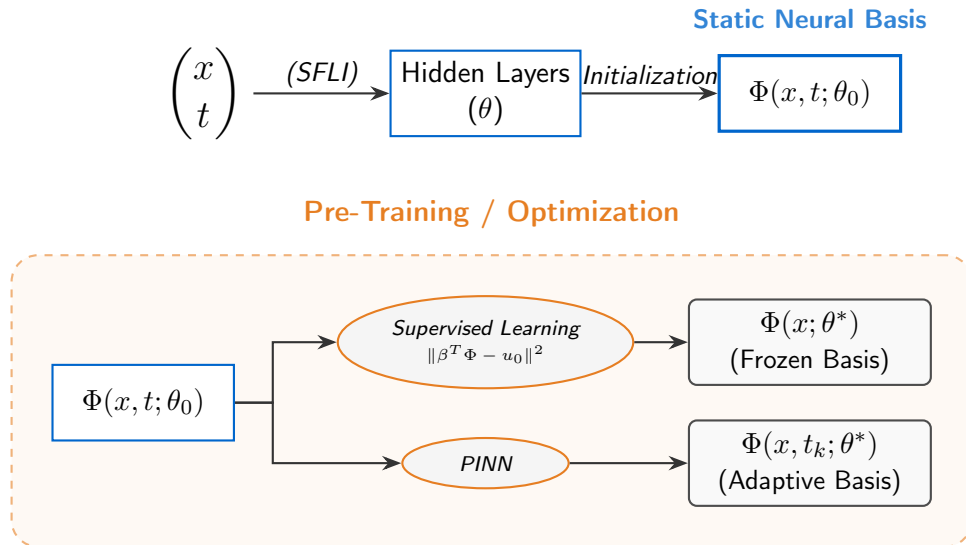


Figure 1: Construction of the neural basis functions.

3.1. Static Neural Basis Functions

In certain regimes, the neural basis can be constructed without iterative training. By carefully initializing the parameters θ , one may generate a trial space with desirable approximation and conditioning properties, thereby avoiding the costly training process. Throughout this subsection, the parameters θ are fixed in time, and only the coefficient vector $\beta(t)$ evolves.

3.1.1. Random Features

The Random Feature paradigm provides a direct mechanism for constructing a neural basis without backpropagation. This idea originates from the extreme learning machine [30] and random Fourier features [31], which establish that randomly sampled hidden nodes yield universal approximation with high probability. This theoretical foundation has been extensively verified across various computational domains [32, 33, 34, 35].

In the Galerkin framework, the internal parameters $\theta = \{W_l, b_l\}_{l=1}^L$ are initialized from a prescribed distribution (e.g., Glorot or Xavier initialization) and subsequently frozen. The resulting trial space is

$$\mathcal{V}_{\theta_{\text{rand}}} = \text{span}\{\phi_1(x; \theta_{\text{rand}}), \dots, \phi_m(x; \theta_{\text{rand}})\}. \quad (29)$$

Under this construction, the nonlinear PDE reduces to a system of ODEs (13) that are linear with respect to the coefficient vector $\beta(t)$.

Although Random Features offer simplicity and avoid training plateaus, their approximation efficiency deteriorates as higher accuracy is required. In practice, the number of neurons must grow rapidly to enrich the functional coverage, which often leads to highly correlated basis functions. Consequently, the mass matrix \mathbf{M} may develop small singular values, resulting in poor conditioning. This limitation motivates the structured initialization discussed next.

3.1.2. Structured First-Layer Initialization (SFLI)

To move beyond purely stochastic initialization, we adopt a deterministic structured construction for the first network layer [36]. For a one-dimensional domain Ω with identity input mapping $z_0 = x$, the first-layer neurons are initialized as

$$(z_1)_j = \sigma(s(x - x_j)), \quad j = 1, \dots, m, \quad (30)$$

where $\{x_j\}_{j=1}^m$ are uniformly distributed points and s controls the slope of the activation.

This structured placement ensures that the initial basis functions are spatially localized and well separated. As a result, the ϵ -rank [29] of the mass matrix is significantly improved compared to purely random sampling. The enhanced spectral structure directly benefits the conditioning of the semi-discrete system.

From a numerical analysis perspective, SFLI can be interpreted as a mesh-free analogue of localized finite element basis functions. The structured placement of neurons provides spatial localization similar to nodal basis functions, while deeper network layers allow nonlinear deformation of these initial features.

3.2. Offline Pre-training Basis

While the SFLI provides a robust general neural basis, the trial space \mathcal{V}_θ can be further enriched by incorporating problem-specific information. We

discuss two refinement strategies: initial-condition alignment and residual-driven pre-training.

3.2.1. Initial-Conditions-Motivated Basis

A natural strategy to customize the functional basis is to align the neural network with the initial state $u_0(x)$ through an offline pre-training stage. This is formulated as the following L^2 minimization problem:

$$\min_{\theta, \beta} \mathcal{L}_{\text{init}}(\theta, \beta) = \frac{1}{N} \sum_{i=1}^N |\beta^T \Phi(x_i; \theta) - u_0(x_i)|^2. \quad (31)$$

Here, β serves as an auxiliary parameter during optimization and is discarded afterward. Upon convergence, the internal parameters are frozen as θ^* , and the trial space becomes

$$\mathcal{V}_{\theta^*} = \text{span}\{\phi_1(x; \theta^*), \dots, \phi_m(x; \theta^*)\}. \quad (32)$$

This procedure produces a problem-adapted frozen basis that accurately captures the initial geometry.

However, two limitations arise. First, if u_0 lies on a low-dimensional manifold, the optimization may reduce basis diversity, leading to a low effective rank of \mathbf{M} . Second, for problems exhibiting significant topological transitions, a basis optimized solely at $t = 0$ may lack sufficient expressivity at later times.

3.2.2. Adaptive Basis Strategy

For problems involving significant topological changes or complex dynamics, a frozen basis may become insufficient for long-term simulations. We therefore introduce an adaptive strategy that combines global feature extraction with local Galerkin evolution. The adaptive DNN-Galerkin procedure consists of three main components:

1. **Global Feature Extraction via Pre-training.** Over the entire time interval $[0, T]$, a PINN is first trained to capture the coarse global dynamics by minimizing the residual functional

$$\mathcal{L}_{\text{res}} = \int_0^T \int_{\Omega} \left| \partial_t u_p - \mathcal{G} \frac{\delta E}{\delta u}(u_p) \right|^2 dx dt, \quad (33)$$

where $u_p(x, t) = \beta^T \Phi(x, t; \theta)$. The optimized hidden-layer parameters θ^* are retained as a global feature extractor. High accuracy is not required at this stage, since the network serves only as a feature extractor for constructing the neural basis.

2. **Time-Local Basis Construction.** Define a set of restart times $\mathcal{T}_{\text{list}} = \{T_0, T_1, \dots, T_K\}$, where $0 = T_0 < T_1 < \dots < T_K = T$. At each restart time T_k , a local neural basis is constructed as

$$\Phi_k(x) = [u_h(x, T_k^-), \phi_1(x, T_k; \theta^*), \dots, \phi_m(x, T_k; \theta^*), 1]^T. \quad (34)$$

The solution on the subinterval $[T_k, T_{k+1}]$ is represented as

$$u_h(x, t) = \beta(t)^T \Phi_k(x), \quad t \in [T_k, T_{k+1}]. \quad (35)$$

For $k = 0$, the representation is initialized by setting $u_h(x, T_0^-) = u_0(x)$ so that the initial condition is satisfied.

3. **Galerkin Evolution.** Within each subinterval $[T_k, T_{k+1}]$, the system is advanced by solving the projected ODE system in the fixed trial space \mathcal{V}_k ,

$$\mathbf{M}_k \frac{d\beta}{dt} = \mathbf{G}_k \mathbf{M}_k^{-1} \mathbf{r}_k(\beta), \quad (36)$$

with the initial coefficient vector $\beta(T_k) = [1, 0, \dots, 0]^T$.

The overall adaptive DNN-Galerkin procedure is summarized in Algorithm 1. An important property of the above adaptive procedure is that the solution is preserved exactly when the neural basis is updated. This feature ensures that the discrete free energy does not experience artificial jumps during basis transitions. As a consequence, the global energy dissipation property of the fully discrete scheme can be established.

Algorithm 1 Adaptive DNN Galerkin Scheme with PINN Pre-training

Require: Initial condition $u_0(x)$, time interval $[0, T]$, subinterval size ΔT , and network architecture.

Ensure: Numerical solution $u(x, t)$ for $t \in [0, T]$.

- 1: **Stage I: PINN Pre-training**
 - 2: Train a standard PINN $u_p(x, t; \theta^*)$ on $[0, T]$ by minimizing the residual loss \mathcal{L}_{res} .
 - 3: Extract the learned parameters θ^* for the hidden layers.
 - 4: **Stage II: Temporal Galerkin Evolution**
 - 5: Initialize $u_0(x, T_0) = u_0(x)$.
 - 6: **for** $k = 0, 1, \dots, K - 1$ **do**
 - 7: **Basis Construction:** Form the augmented basis at T_k : $\Phi_k(x) = [u_h(x, T_k), \phi_1(x, T_k; \theta^*), \dots, \phi_m(x, T_k; \theta^*), 1]^T$.
 - 8: **ODE Assembly:** Construct the mass matrix \mathbf{M}_k and residual vector \mathbf{r}_k .
 - 9: **Time Stepping:** Solve the ODE system over $[T_k, T_{k+1}]$ using structure-preserving time integrator (e.g., IMEX-RK2):
 $\mathbf{M}_k \frac{d\beta}{dt} = \mathbf{G}_k \mathbf{M}_k^{-1} \mathbf{r}_k(\beta)$, $\beta(T_k) = [1, 0, \dots, 0]^T$.
 - 10: **Update:** Set $u_h(x, t) = \beta(t)^T \Phi_k(x)$ for $t \in [T_k, T_{k+1}]$.
 - 11: **end for**
-

Theorem 2 (Global discrete energy dissipation of the adaptive DNN-G scheme). *Let $\{t_n\}_{n=0}^{N_t}$ be the fully discrete time sequence and $\{T_k\}_{k=0}^K \subseteq \{t_n\}_{n=0}^{N_t}$ the set of basis update times. Assume that on each subinterval $[T_k, T_{k+1}]$ the semi-discrete DNN-Galerkin system is advanced by a fully discrete time integrator that satisfies the discrete energy dissipation property (for example, the IMEX-RK2 scheme (27)).*

Then the adaptive DNN-Galerkin solution $u_h^n := u_h(\cdot, t_n)$ satisfies the global discrete energy dissipation law

$$E[u_h^{n+1}] \leq E[u_h^n], \quad \forall n \geq 0. \quad (37)$$

That is, the discrete free energy is monotonically non-increasing over the entire simulation, including across the basis update points.

Proof. On each subinterval $[T_k, T_{k+1}]$, the neural trial space \mathcal{V}_k remains fixed. The Galerkin discretization then yields a finite-dimensional dynamical system for the coefficient vector $\beta(t)$. The resulting evolution equation can be

written in the gradient flow form

$$\dot{\beta} = \mathbf{Q}\nabla_{\beta}\mathcal{E}(\beta), \quad (38)$$

where $\mathcal{E}(\beta) = E[u_h]$ denotes the discrete energy and $\mathbf{Q} = \mathbf{M}^{-1}\mathbf{G}\mathbf{M}^{-1}$ is a symmetric negative semidefinite matrix determined by the mass matrix of the basis functions. Therefore, the semi-discrete system is itself a finite-dimensional gradient flow.

By assumption, the time integration scheme applied to this system satisfies a discrete energy dissipation property. Consequently, the numerical solution satisfies

$$E[u_h^{n+1}] \leq E[u_h^n], \quad (39)$$

for all time steps $t_n, t_{n+1} \in [T_k, T_{k+1}]$.

Next consider a basis update time T_k . The adaptive construction Φ_k includes the previous numerical solution $u_h(\cdot, T_k^-)$ as the first basis function of the new trial space. With the initial coefficient vector

$$\beta(T_k^+) = [1, 0, \dots, 0]^T, \quad (40)$$

the solution is preserved exactly,

$$u_h(x, T_k^+) = \beta(T_k^+) \cdot \Phi_k(x) = u_h(x, T_k^-). \quad (41)$$

Consequently, the discrete energy is continuous at the update time,

$$E[u_h(\cdot, T_k^+)] = E[u_h(\cdot, T_k^-)]. \quad (42)$$

Combining the energy dissipation within each subinterval with the continuity of the energy at the update points yields the global estimate

$$E[u_h^{n+1}] \leq E[u_h^n], \quad \forall n \geq 0. \quad (43)$$

□

4. Numerical Experiments

4.1. Settings

Unless otherwise specified in the individual examples, all neural networks considered in this work are fully-connected feedforward networks with hyperbolic tangent (tanh) activation functions. The resulting semi-discrete

Galerkin system (13) is solved using a second-order stabilized Implicit-Explicit Runge-Kutta method (IMEX-RK2) [7] with a uniform time step size $\Delta t = 10^{-3}$. Spatial integrals in the Galerkin formulation are evaluated using Gaussian quadrature rules or Monte Carlo integration for mass matrix \mathbf{M} and stiffness matrix \mathbf{K} , where

$$\mathbf{M}_{ij} = \int_{\Omega} \phi_i \phi_j dx, \quad \mathbf{K}_{ij} = \int_{\Omega} \nabla \phi_i \cdot \nabla \phi_j dx. \quad (44)$$

Neural basis functions are constructed from networks whose weights are initialized using the LeCun initialization, and biases are initialized to zero, resulting in random neural features. When specified, the structured first-layer initialization (SFLI) is applied to the first hidden layer.

When pre-training is employed, it corresponds to a standard Physics-Informed Neural Network (PINN) training procedure, which also serves as a baseline method in the numerical comparisons. The PINN training is performed using the Adam optimizer for 30000 steps, with an initial learning rate of 10^{-3} and a cosine-decay learning-rate schedule. Training samples are uniformly and randomly generated in the spatio-temporal domain and regenerated at every optimization step.

To mitigate the ill-conditioning of the mass matrix caused by nearly linearly dependent neural basis functions, we apply a discrete orthogonalization procedure based on truncated singular value decomposition. At each restart time T_k , the raw neural basis functions are evaluated at Gaussian quadrature nodes and assembled into a weighted basis matrix. Singular values below a prescribed tolerance relative to the largest singular value are truncated to construct an approximately L^2 -orthonormal basis. The initial condition basis function $u_h(x, T_k^-)$ is explicitly preserved in the resulting augmented basis. This preprocessing step improves the conditioning of the semi-discrete system while preserving the approximation capacity of the trial space.

The numerical accuracy is evaluated using the relative L^2 error

$$e(t) = \frac{\|u_h(\cdot, t) - u_{\text{ref}}(\cdot, t)\|_{L^2(\Omega)}}{\|u_{\text{ref}}(\cdot, t)\|_{L^2(\Omega)}}, \quad (45)$$

where u_{ref} denotes a highly resolved reference solution or an analytical solution. For the Allen–Cahn equations, the reference solutions are computed using spectral methods in space combined with the fourth-order exponential time-differencing Runge–Kutta scheme [37].

The network architectures and example-specific training hyperparameters are summarized in Table 1.

Table 1: Summary of network architectures and example-specific hyperparameters for each numerical example.

Example	Hidden Layers	Batch Size	Opt. Steps	Quad. Pts	Subintervals ($\mathcal{T}_{\text{list}}$)
2 (5D Heat)	[50, 50, 50, 900]	10,000	30,000*	12/dim	[0.0, 1.0]
2 (10D Heat)	[50, 50, 50, 900]	10,000	30,000*	$N_{\text{MC}}=10^4$ to 10^7	[0.0, 1.0]
3 (1D AC)	[128, 128, 128]	8,192	30,000	1024	{0.0, 0.2, ..., 1.0}
4 (2D AC, Bubble)	[50, 50, 50, 64/1024]	15,000	30,000*	128/dim	{0.0, 0.1, ..., 1.0}
5 (2D AC, Star)	[50, 50, 50, 1024]	20,000	30,000*	128/dim	{0.0, 0.5, ..., 5.0} [†]
6 (2D AC, Random)	[50, 50, 50, 1024]	10,000	30,000*	128/dim	{0.0, 0.1, ..., 1.0} [†]
7 (1D CH)	[128, 128, 128]	8,192	30,000	1024	{0.0, 0.005, 0.01, 0.015, 0.04, 0.08, 0.12, 0.16, 0.2}

Note: All networks use tanh activations. The optimization steps correspond to the number of Adam iterations. *Indicates an additional 1500 L-BFGS refinement iterations with the batch size increased by a factor of four. The subintervals ($\mathcal{T}_{\text{list}}$) indicate the restart points for the adaptive basis in time evolution. [†]For the untrained SFLI-DNN-G scheme in Ex. 5 and 6, a single global interval ([0.0, 5.0] and [0.0, 1.0], respectively) is employed instead of adaptive subintervals.

4.2. Heat Equation

To examine the high-dimensional behavior and temporal accuracy of the proposed DNN-Galerkin method, we consider the d -dimensional heat equation, which serves as a prototypical linear L^2 gradient flow. As the spatial dimension increases, classical mesh-based discretizations suffer from the exponential growth of grid points, making them computationally prohibitive. This example therefore provides a natural benchmark for assessing the approximation efficiency of neural trial spaces in high-dimensional settings.

Example 2 (High-dimensional Heat Equation). Consider the d -dimensional heat equation on the domain $\Omega = [-0.5, 0.5]^d$ with homogeneous Dirichlet boundary conditions:

$$u_t = \frac{1}{d\pi^2} \Delta u, \quad \mathbf{x} \in \Omega, \quad t \in [0, 1], \quad (46)$$

which corresponds to the L^2 gradient flow associated with the Dirichlet energy

$$E[u] = \frac{1}{2} \int_{\Omega} |\nabla u|^2 d\mathbf{x}. \quad (47)$$

The initial condition is chosen as:

$$u_0(\mathbf{x}) = \prod_{i=1}^d \cos(\pi x_i), \quad (48)$$

for which the exact solution reads:

$$u(\mathbf{x}, t) = e^{-t} \prod_{i=1}^d \cos(\pi x_i). \quad (49)$$

The semi-discrete system (13) is integrated using second- and third-order Diagonally Implicit Runge-Kutta (DIRK) schemes [38]. The neural trial space consists of $m = 900$ frozen random features generated from a fully connected network. Homogeneous Dirichlet boundary conditions are enforced by the modified basis

$$\tilde{\phi}_i(\mathbf{x}; \theta) = \phi_i(\mathbf{x}; \theta) \prod_{j=1}^d \left(\frac{1}{4} - x_j^2 \right).$$

All spatial integrals are evaluated using Gaussian quadrature for $d = 5$ and Monte Carlo integration for higher dimensions.

Figure 2 shows the temporal convergence results for $d = 5$. The DNN-G scheme follows the expected convergence orders of the underlying DIRK integrators. This confirms that the Galerkin projection preserves the temporal accuracy of the time discretization within the neural trial space.

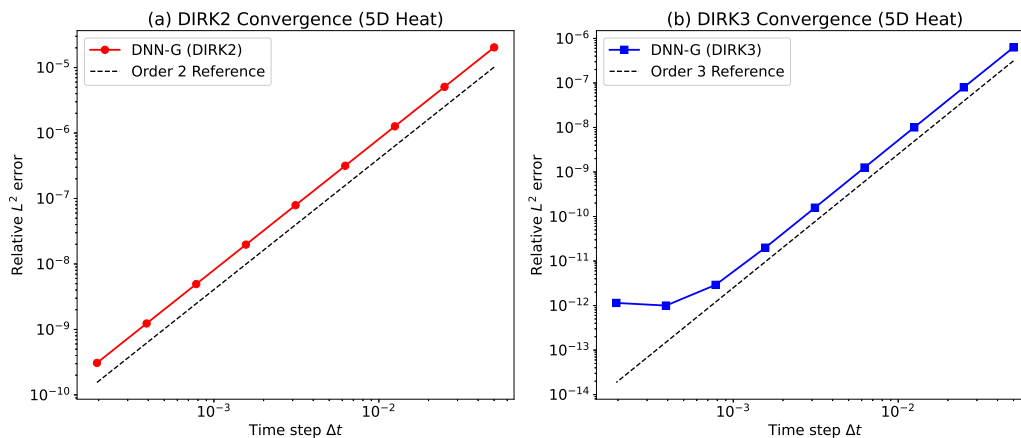


Figure 2: Temporal convergence test for the 5D heat equation (Example 2, $d = 5$). (a) The second-order DIRK scheme (DIRK2) exhibits an $O(\Delta t^2)$ convergence rate. (b) The third-order DIRK scheme (DIRK3) achieves $O(\Delta t^3)$ accuracy, eventually reaching a plateau due to spatial discretization limits.

For the DIRK3 scheme, the error curve eventually reaches a plateau as Δt decreases, indicating a transition from a time-discretization-dominated regime to a spatial-approximation-dominated regime. The plateau level reflects the intrinsic approximation error of the neural trial space. To further assess the accuracy, we compare the relative L^2 error at $t = 1$ with a standard PINN under the same setup. The PINN attains a relative L^2 error of 1.54×10^{-4} , whereas the DNN-G method achieves 2.57×10^{-11} when $d = 5$. This result highlights the accuracy advantage of the Galerkin formulation.

We further extend the test to a higher-dimensional regime ($d = 10$), where the spatial integrals in the variational formulation are approximated using Monte Carlo integration. In this setting, the statistical accuracy of the sampled mass matrix becomes a dominant source of spatial error.

As shown in Fig. 3, once the number of quadrature points reaches $N_{MC} = 10^6$, the DNN-G scheme consistently outperforms the standard PINN. Despite the statistical noise introduced by high-dimensional integration, the DNN-G framework preserves the gradient-flow structure. Its energy dissipation closely follows the analytical trajectory, whereas the optimization-based PINN exhibits noticeable deviations.

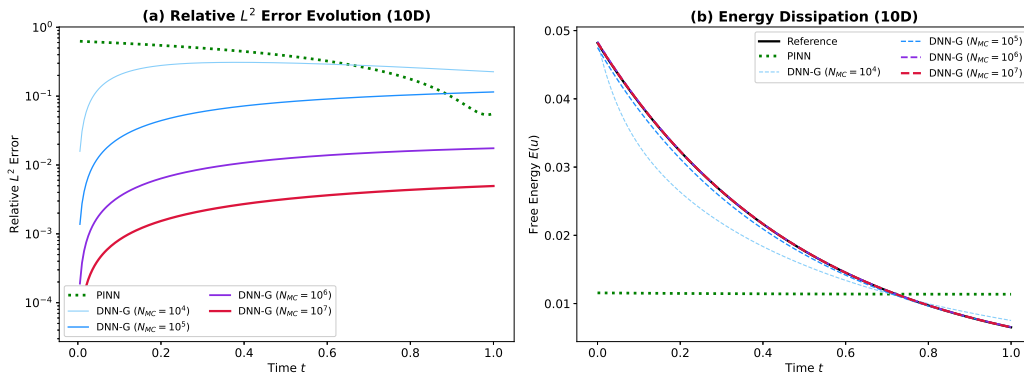


Figure 3: Quantitative comparison for the 10D heat equation (Example 2, $d = 10$). (a) Relative L^2 error evolution. (b) Energy dissipation. The standard PINN (green dotted line) is compared against the DNN-G scheme, where the integrals are approximated using varying numbers of Monte Carlo points ($N_{MC} = 10^4$ to 10^7).

We remark that this level of accuracy is obtained with only $m = 900$ basis functions. For comparison, a finite difference discretization with approximately the same number of degrees of freedom ($4^5 \approx 1024$ in five dimensions and $2^{10} \approx 1024$ in ten dimensions) would correspond to a mere four and two

grid points per spatial direction, respectively. This illustrates the efficiency of neural trial spaces for high-dimensional problems.

4.3. Allen–Cahn Equation

The Allen–Cahn equation is a classical phase-field model describing the L^2 gradient flow of the Ginzburg–Landau free energy [39, 40]. It serves as a prototypical nonlinear dissipative system for studying phase separation and interface dynamics. Given the Ginzburg–Landau free energy:

$$E[u] = \int_{\Omega} \left(\frac{\epsilon^2}{2} |\nabla u|^2 + F(u) \right) dx, \quad (50)$$

where $F(u) = \frac{1}{4}(u^2 - 1)^2$ is the double-well potential, the corresponding L^2 gradient flow reads:

$$u_t = \epsilon^2 \Delta u - \kappa f(u), \quad f(u) = F'(u) = u^3 - u. \quad (51)$$

This equation models the phase separation process, where the system evolves towards minimizing the free energy by forming interfaces between the two stable phases $u = \pm 1$.

4.3.1. 1D Case

Example 3 (1D Allen–Cahn equation). We consider the one-dimensional problem:

$$u_t = \epsilon^2 u_{xx} - \kappa f(u), \quad x \in [-1, 1], \quad t \in [0, 1], \quad (52)$$

where $\epsilon = 0.01$ and $\kappa = 5$. The initial condition is set as $u_0(x) = x^2 \cos(\pi x)$.

In this example, the initial condition is enforced via a hard constraint: $u_p(x, t; \theta) = u_0(x) + t \cdot \mathcal{N}(x, t; \theta)$. The neural basis functions are pre-trained via this PINN-based procedure, after which the adaptive DNN-Galerkin (ADNN-G) framework is employed for time evolution. To discretize the semi-discrete system (13), we consider two representative schemes.

- **Stabilized Semi-Implicit (SSI1) Scheme.** A first-order scheme treating the diffusion term implicitly and the nonlinear term explicitly. A linear stabilization term with parameter $S > 0$ is introduced to enhance energy stability:

$$\mathbf{M} \frac{\beta^{n+1} - \beta^n}{\Delta t} = -\epsilon^2 \mathbf{K} \beta^{n+1} - \mathbf{g}(\beta^n) - S \mathbf{M} (\beta^{n+1} - \beta^n), \quad (53)$$

where

$$g_j(\beta^n) = \int_{-1}^1 f(u_h(x, t_n)) \phi_j(x) dx. \quad (54)$$

- **Energy-Stabilized IMEX-RK2 Scheme (27).**

Figure 4 presents the temporal convergence results. Both schemes achieve their expected theoretical orders, indicating that the Galerkin projection preserves the temporal accuracy of the underlying integrators. As in the heat equation example, the IMEX-RK2 error eventually reaches a plateau, corresponding to the spatial approximation limit of the neural basis. In the following experiments, we adopt IMEX-RK2 due to its higher temporal accuracy.

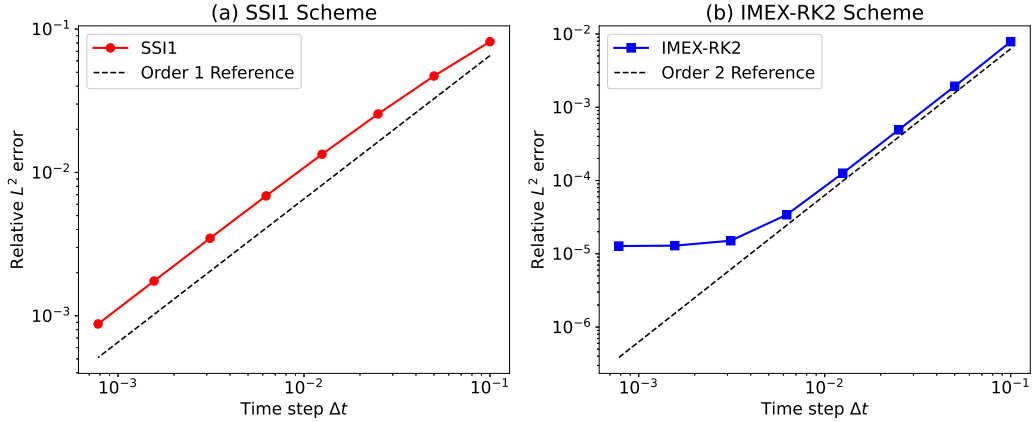


Figure 4: Temporal convergence test for the 1D Allen-Cahn equation (Example 3) comparing the SSI1 and IMEX-RK2 schemes with adaptive DNN Galerkin method.

Figure 5 compares the DNN-Galerkin solution, a standard PINN, and a spectral reference solution. Panels (a) and (b) show the solution profiles at $t = 0.2$ and $t = 1.0$. While the PINN captures the overall phase transition, visible discrepancies appear near the sharp interface. The ADNN-G solution remains in close agreement with the spectral reference throughout the evolution.

The relative L^2 error evolution in Fig. 5(c) demonstrates that the DNN-G method maintains consistently lower errors over time. More importantly, Fig. 5(d) verifies the discrete energy dissipation property. The DNN-G scheme exhibits monotone decay of the free energy, consistent with the gradient flow structure. In contrast, the PINN solution shows noticeable energy

gaps, reflecting the absence of structural constraints in residual-based training.

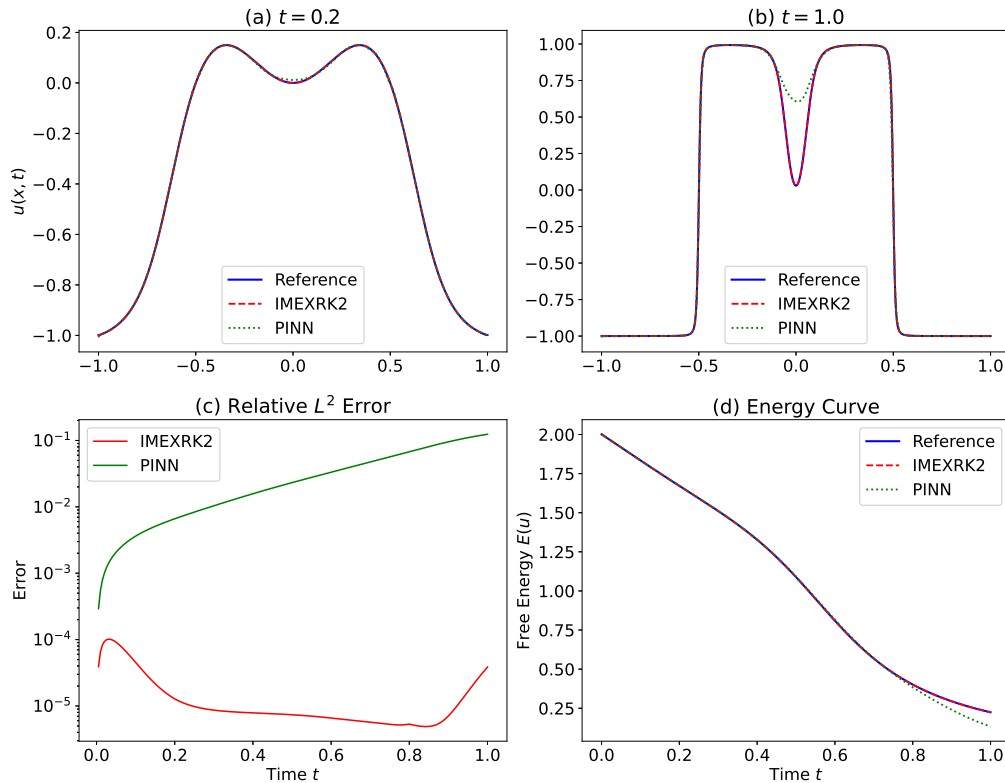


Figure 5: Numerical results for the 1D Allen–Cahn equation (Example 3). (a)–(b) Comparison of solution profiles $u(x, t)$. (c) Temporal evolution of the relative L^2 error. (d) Free energy dissipation $E(u)$ curves.

4.3.2. 2D Case

Example 4 (The evolution of two circular bubbles). We consider the two-dimensional Allen–Cahn equation on $\Omega = [-0.5, 0.5]^2$:

$$u_t = \epsilon^2 \Delta u - \kappa f(u), \quad (x, y) \in \Omega, \quad t \in [0, 1], \quad (55)$$

where $\epsilon = 0.05$, $\kappa = 5$. The initial condition describes two separate circular bubbles:

$$u_0(x, y) = \max \left\{ \tanh \left(\frac{R - d_1}{\epsilon} \right), \tanh \left(\frac{R - d_2}{\epsilon} \right) \right\}, \quad (56)$$

where $R = 0.15$ is the radius, and $d_{1,2} = \sqrt{(x \pm 0.21)^2 + y^2}$.

Figure 6 illustrates the evolution process of the proposed adaptive DNN Galerkin method (ADNN-G), the standard PINN, and the traditional spectral method under equivalent degrees of freedom (DoF). Driven by mean curvature, the two nearby interfaces gradually coalesce, which serves as a stringent test for accurately resolving high-curvature dynamics.

With $m = 1024$ adaptive neural basis functions, the proposed ADNN-G method accurately captures the merging process and closely matches the high-resolution spectral reference solution. Among all tested methods, ADNN-G with DoF = 1024 achieves the highest accuracy and reproduces the energy dissipation curve almost identically to the reference solution.

For a fair comparison under similar degrees of freedom, we further compare ADNN-G with DoF = 64 against the spectral method with DoF = $32^2 = 1024$. Although the two solutions appear visually similar in the snapshots, the ADNN-G solution aligns better with the energy dissipation curve. This indicates that the adaptive neural basis functions provide a more efficient representation of the evolving interface dynamics. In contrast, both the standard PINN and the spectral method with DoF = 8^2 fail to capture the interface coalescence within the simulated time horizon, indicating insufficient resolution to represent the strongly nonlinear dynamics.

The quantitative comparison in Fig. 7 further confirms these observations. As shown in Fig. 7(a), ADNN-G with DoF = 1024 achieves the smallest relative L^2 errors among all methods. Meanwhile, ADNN-G with only DoF = 64 attains an accuracy comparable to the spectral method with DoF = 32^2 , despite using significantly fewer degrees of freedom. This clearly demonstrates a super-approximation effect: while fixed trigonometric bases require substantially higher resolution to resolve sharp interfaces, the adaptive neural basis functions automatically concentrate in high-gradient regions.

Additionally, the energy dissipation curves in Fig. 7(b) show that both ADNN-G schemes follow the reference thermodynamic path more faithfully than the competing methods, highlighting the structure-preserving property of the proposed framework.

Example 5 (Non-uniform curvature-driven motion). To further evaluate the ability of DNN-G to resolve phase-field dynamics with spatially varying curvature, we consider a star-shaped interface defined in polar coordinates

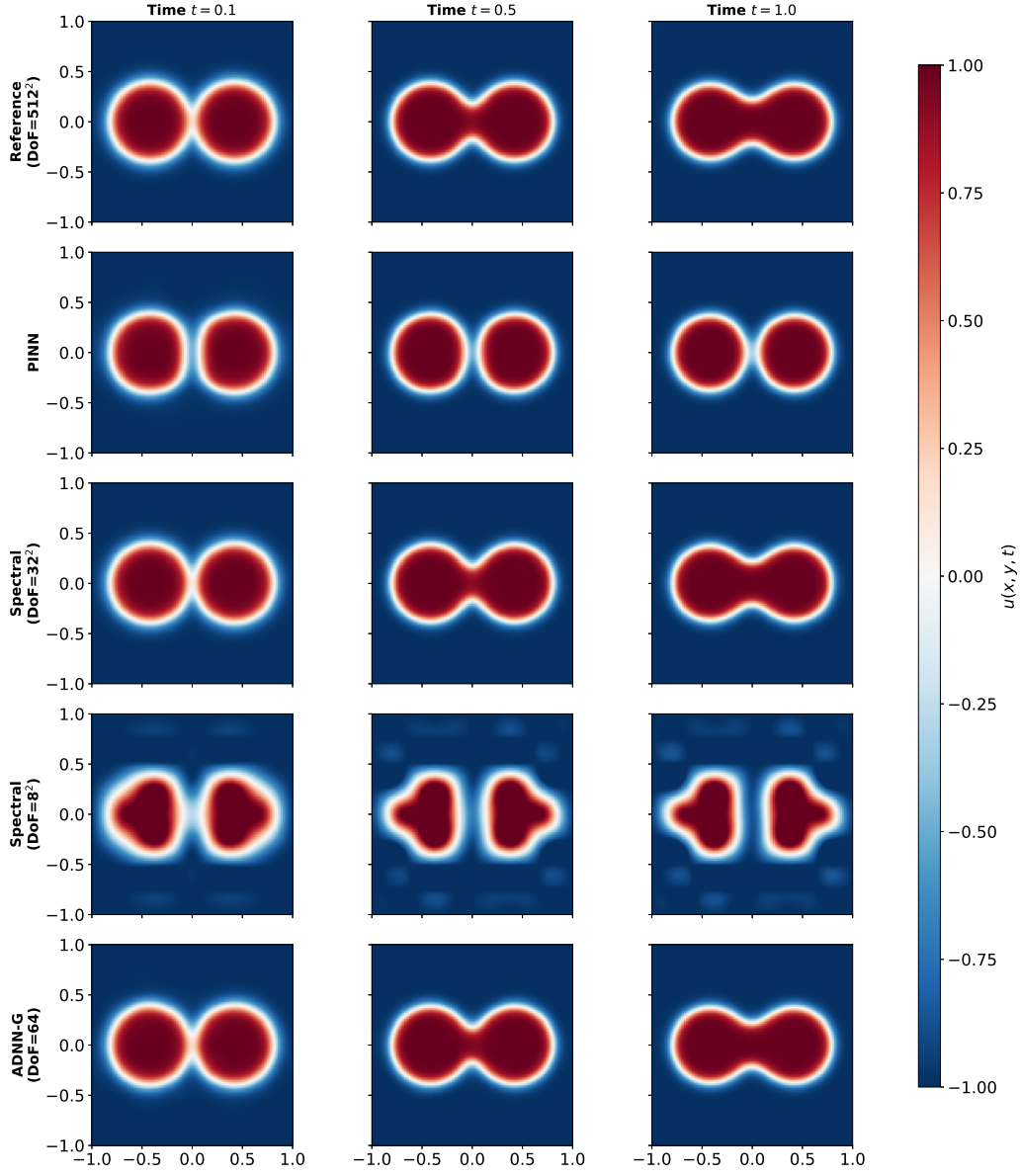


Figure 6: Snapshots of the phase-field $u(x, y, t)$ evolution for the merging process of two circular interfaces (Example 4). Rows from top to bottom: Reference spectral solution (DoF = 512^2), standard PINN, spectral solution (DoF = 32^2 and 8^2), and the proposed adaptive DNN Galerkin (ADNN-G, DoF = 64) scheme at $t = 0.1, 0.5$, and 1.0 .

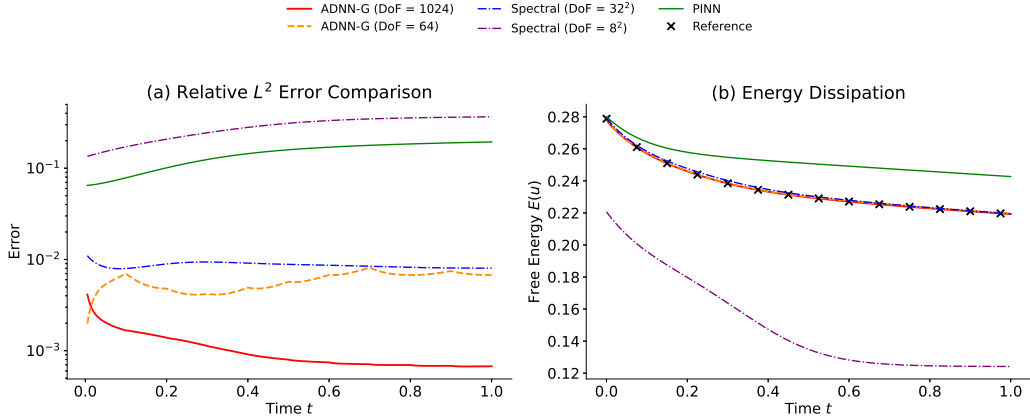


Figure 7: Quantitative comparison for the 2D Allen–Cahn equation (Example 4). (a) Relative L^2 error evolution (excluding $t = 0$ to highlight dynamical differences). (b) Free energy dissipation $E(u)$ comparison.

(r, θ) :

$$u_0(r, \theta) = \tanh\left(\frac{R_0 + \delta \cos(k\theta) - r}{\sqrt{2}\epsilon}\right), \quad (57)$$

where $R_0 = 0.25$, $\delta = 0.05$, and $k = 5$. The parameters $\epsilon = 0.05$ and $\kappa = 5$ are the same as those in Example 4.

The evolution of the star-shaped interface is presented in Fig. 8. As illustrated in the snapshots, the standard PINN exhibits a non-physical failure, while the RF-DNN-G scheme also struggles to capture the correct dynamics, with the solution remaining close to the initial condition. In contrast, both ADNN-G and SFLI-DNN-G accurately reproduce the morphological evolution, capturing the relaxation from the star-shaped interface toward the circular equilibrium.

Quantitative evaluations in Fig. 9 corroborate these observations. As shown in Fig. 9(a), the relative L^2 errors of SFLI-DNN-G and ADNN-G remain significantly lower than those of PINN and RF-DNN-G throughout the simulation. The free energy evolution in Fig. 9(b) further illustrates the structure-preserving property of the Galerkin formulation. Both SFLI-DNN-G and ADNN-G closely follow the reference energy dissipation curve. Although RF-DNN-G yields poor predictive accuracy, its Galerkin structure ensures that the energy remains non-increasing. In contrast, the PINN solution exhibits both large errors and non-physical energy growth, highlighting

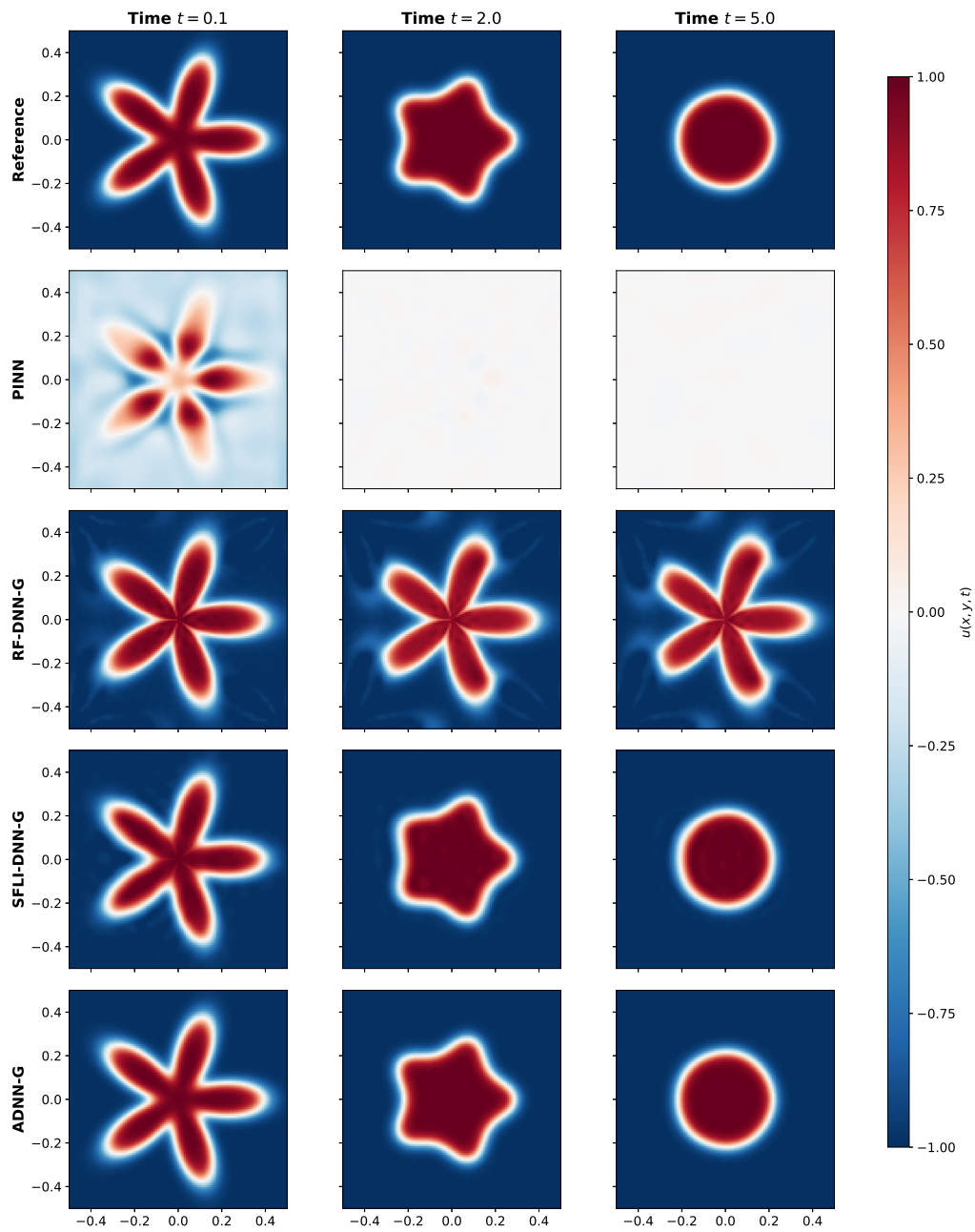


Figure 8: Snapshots of the phase-field evolution for a star-shaped interface (Example 5) at $t = 0.1, 2.0$, and 5.0 . From top to bottom: Reference spectral solution, standard PINN, random feature based DNN-Galerkin scheme (RF-DNN-G), SFLI based DNN-Galerkin scheme (SFLI-DNN-G), and the adaptive DNN-Galerkin scheme (ADNN-G).

the difficulty of directly minimizing residual losses for stiff gradient flows.

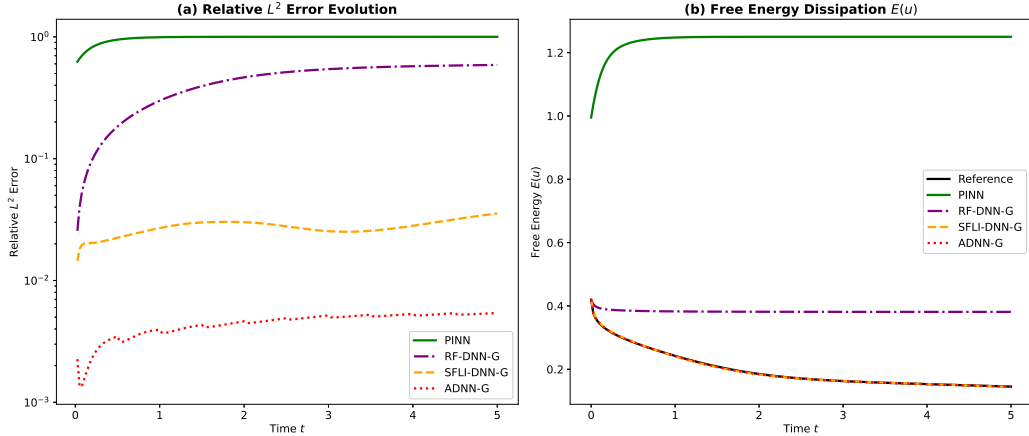


Figure 9: Quantitative comparison for the star-shaped interface relaxation (Example 5). (a) Relative L^2 error evolution. (b) Free energy dissipation $E(u)$.

A key insight from this example is the essential role of basis adaptivity. The poor performance of RF-DNN-G indicates that a structure-preserving Galerkin projection alone cannot compensate for an inadequate trial space. In contrast, the superior accuracy of ADNN-G compared with SFLI-DNN-G highlights a synergistic effect: although direct PINN optimization fails to recover the correct macroscopic dynamics, the training process implicitly extracts informative nonlinear features that align the neural basis functions with the underlying solution manifold. The subsequent Galerkin projection then exploits these learned bases to accurately recover the dynamics. This observation suggests that while residual minimization may struggle as a standalone solver for stiff gradient flows, it can serve as an effective mechanism for constructing an expressive low-dimensional trial space for Galerkin-based solvers.

We further examine the proposed DNN Galerkin framework in a more demanding regime: coarsening dynamics initiated from a random state. This setup involves multiple simultaneous coalescence events and rapidly evolving multi-scale structures, posing a stringent test for neural-network-based PDE solvers. To the best of our knowledge, existing neural-network approaches have not demonstrated stable and physically consistent simulations of the Allen–Cahn equation starting from fully random initial data, making this scenario particularly challenging.

Example 6 (Coarsening from a random initial condition). The governing equation and parameters are the same as in Example 4. The initial condition is sampled from a uniform distribution:

$$u_0(x, y) \sim \mathcal{U}(-1, 1), \quad (x, y) \in \Omega. \quad (58)$$

Since a purely random field lacks spatial regularity, we project u_0 onto a finite-dimensional spectral basis to obtain a smooth but highly oscillatory initial configuration.

The numerical results in Fig. 10 and Fig. 11 demonstrate a clear contrast between optimization-based and Galerkin-based approaches. The standard PINN struggles to represent the rapidly evolving multi-scale structures, leading to noticeable deviations from the reference solution even at early times. The RF-DNN-G scheme exhibits intermediate performance: although the Galerkin projection improves the qualitative topological evolution compared with PINN, its fixed random trial space lacks sufficient expressivity to accurately resolve the interface dynamics. In contrast, both SFLI-DNN-G and ADNN-G successfully reproduce the coarsening process, capturing successive interface mergers while maintaining consistent energy dissipation.

These results highlight the importance of constructing an expressive trial space for complex coarsening dynamics. Compared with the inadequate expressivity of random features, the neural basis generated by SFLI already provides an effective static representation of the solution manifold.

More importantly, the results emphasize that the structure-preserving Galerkin formulation plays a central role in ensuring physical consistency. By embedding the gradient-flow structure into the numerical scheme, the DNN-Galerkin framework guarantees stable energy dissipation even during highly nonlinear, multi-scale evolution, whereas direct residual minimization alone struggles to maintain such physical properties.

4.4. Cahn–Hilliard equation

We further evaluate the proposed framework on the Cahn–Hilliard equation, which describes the H^{-1} gradient flow of the Ginzburg–Landau free energy [41]. Compared with the Allen–Cahn equation, the Cahn–Hilliard model involves fourth-order spatial derivatives and mass conservation, resulting in significantly stronger numerical stiffness. This example therefore provides a stringent test for neural-network-based solvers for high-order phase-field dynamics.

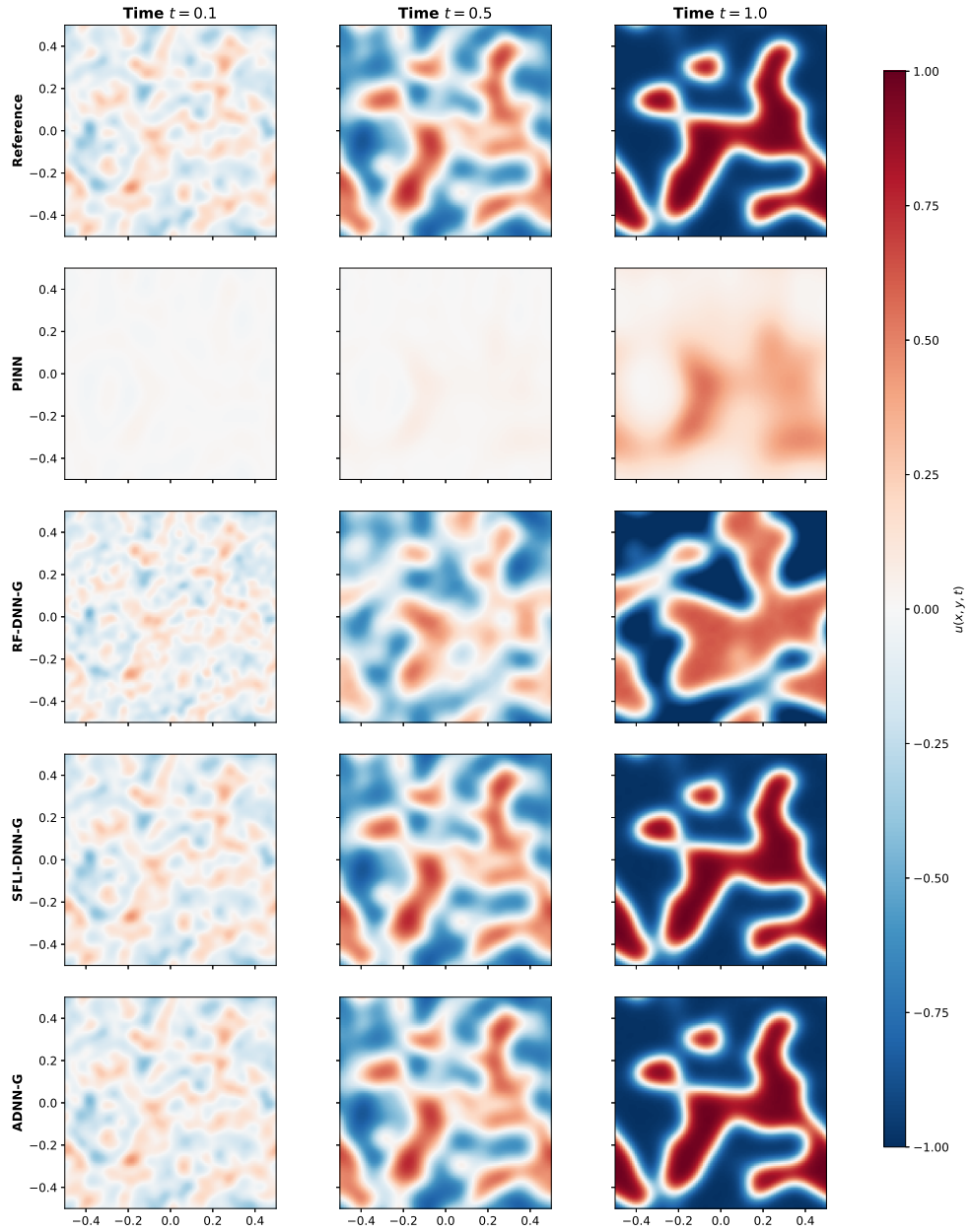


Figure 10: Snapshots of the phase-field $u(x, y, t)$ evolution for the random initial condition (Example 6) at $t = 0.1, 0.5$, and 1.0 . From top to bottom: Reference spectral solution, standard PINN, random feature based DNN-Galerkin scheme (RF-DNN-G), SFLI based DNN-Galerkin scheme (SFLI-DNN-G), and the adaptive DNN-Galerkin scheme (ADNN-G).

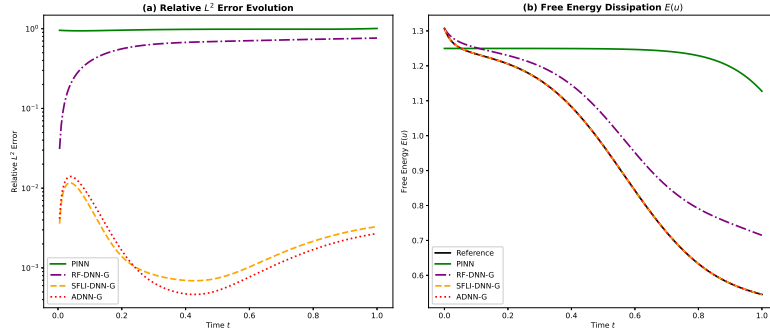


Figure 11: Quantitative comparison for the coarsening dynamics from a random initial condition (Example 6). (a) Relative L^2 error evolution. (b) Free energy dissipation $E(u)$ comparison.

Example 7 (Cahn–Hilliard equation). Consider the one-dimensional Cahn–Hilliard equation

$$u_t = -\epsilon^2 u_{xxxx} + (u^3 - u)_{xx}, \quad x \in [-1, 1], \quad t \in [0, 1]. \quad (59)$$

The initial condition is $u_0(x) = \cos(\pi x)$. To examine both mild and stiff regimes, two interfacial width parameters are considered: $\epsilon = 0.1$ and $\epsilon = 0.01$.

For time integration, we employ the similar IMEX-RK2 scheme used in the Allen–Cahn example, which can be found in [7].

Figure 12 shows the spatiotemporal evolution of the solution using x - t contour plots. For the mild regime ($\epsilon = 0.1$), both PINN and ADNN-G capture the overall phase separation pattern. Fig. 13 further indicates that ADNN-G maintains smaller relative L^2 errors throughout the simulation.

The difference becomes more significant in the stiff regime ($\epsilon = 0.01$), where the interface width is much smaller and the dynamics are highly stiff. In this case, the standard PINN fails to accurately resolve the evolution due to the severe stiffness induced by the fourth-order spatial derivatives, leading to large approximation errors and non-physical energy behavior. In contrast, the ADNN-G scheme remains stable and accurately reproduces the phase separation dynamics.

This robustness stems from the weak Galerkin formulation, which transfers the high-order derivatives onto the basis functions through integration by parts. As a result, the regularity requirements imposed on the neural network representation are significantly relaxed.

The quantitative results in Fig. 13 further demonstrate the advantage of the proposed method. While the PINN solution in the stiff regime exhibits energy stagnation and noticeable fluctuations, the ADNN-G scheme preserves the correct monotonic free-energy dissipation and closely follows the reference solution throughout the evolution.

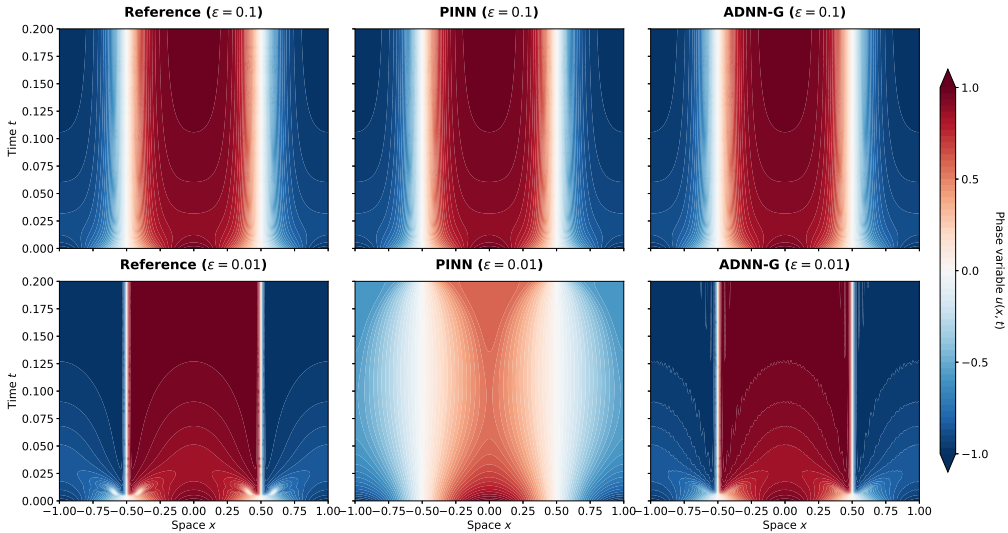


Figure 12: Spatiotemporal evolution of the phase variable $u(x, t)$ for the Cahn–Hilliard dynamics (Example 7) with $\epsilon = 0.1$ (top row) and $\epsilon = 0.01$ (bottom row). From left to right: Reference spectral solution, standard PINN, and the proposed ADNN-G scheme.

5. Conclusion

In this work, we proposed a structure-preserving deep neural network Galerkin framework for nonlinear dissipative partial differential equations. By embedding neural networks into a Galerkin projection formulation, the method preserves the variational structure of gradient flows and guarantees discrete energy dissipation throughout the numerical evolution.

Extensive numerical experiments demonstrate that the proposed approach provides improved accuracy and robustness compared with optimization-based neural PDE solvers, particularly for high-dimensional and multi-scale dynamics. Under comparable degrees of freedom, the DNN-Galerkin method can also outperform classical spectral discretizations, indicating that neural

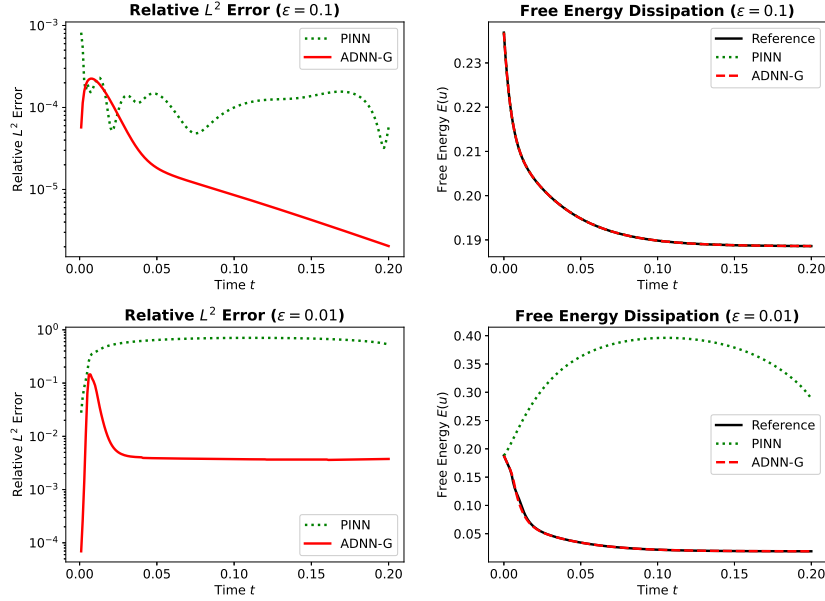


Figure 13: Relative L^2 error and free-energy dissipation for the Cahn–Hilliard dynamics (Example 7) with $\epsilon = 0.1$ (top row) and $\epsilon = 0.01$ (bottom row).

trial spaces offer strong approximation capability for complex evolving structures.

An important observation from this study is that the effectiveness of neural PDE solvers is largely determined by the quality of the induced trial space rather than by the optimization procedure itself. Even when direct neural training fails to converge to a satisfactory solution, properly constructed neural basis functions can still provide efficient approximation spaces when combined with a structure-preserving Galerkin projection.

These findings suggest a different perspective on neural approaches to scientific computing: deep neural networks can serve as adaptive basis generators within structure-aware numerical discretization frameworks. Future work will extend the proposed methodology to more challenging dissipative systems, including stiff gradient flows, higher-dimensional problems, and kinetic equations, further exploring neural representations as flexible approximation spaces for large-scale PDE simulations.

Acknowledgments

This work is supported by the National Science Foundation of China (No.12271240, 12426312), the fund of the Guangdong Provincial Key Laboratory of Computational Science and Material Design, China (No.2019B030301001), the Shenzhen Natural Science Fund (RCJC20210609103819018), and the Zhuhai Innovation and Entrepreneurship Team Project (2120004000498).

References

- [1] J. Shen, C. Wang, X. Wang, S. M. Wise, Second-order Convex Splitting Schemes for Gradient Flows with Ehrlich–Schwoebel Type Energy: Application to Thin Film Epitaxy, *SIAM Journal on Numerical Analysis* 50 (1) (2012) 105–125. doi:10.1137/110822839.
- [2] W. Chen, S. Conde, C. Wang, X. Wang, S. M. Wise, A Linear Energy Stable Scheme for a Thin Film Model Without Slope Selection, *Journal of Scientific Computing* 52 (3) (2012) 546–562. doi:10.1007/s10915-011-9559-2.
- [3] J. Shen, J. Xu, J. Yang, The scalar auxiliary variable (SAV) approach for gradient flows, *Journal of Computational Physics* 353 (2018) 407–416. doi:10.1016/j.jcp.2017.10.021.
- [4] J. Shen, J. Xu, J. Yang, A New Class of Efficient and Robust Energy Stable Schemes for Gradient Flows, *SIAM Review* 61 (3) (2019) 474–506. doi:10.1137/17M1150153.
- [5] X. Yang, J. Zhao, Q. Wang, J. Shen, Numerical approximations for a three-component Cahn–Hilliard phase-field model based on the invariant energy quadratization method, *Mathematical Models and Methods in Applied Sciences* 27 (11) (2017) 1993–2030. doi:10.1142/S0218202517500373.
- [6] G. Beylkin, J. M. Keiser, L. Vozovoi, A New Class of Time Discretization Schemes for the Solution of Nonlinear PDEs, *Journal of Computational Physics* 147 (2) (1998) 362–387. doi:10.1006/jcph.1998.6093.
- [7] Z. Fu, T. Tang, J. Yang, Energy diminishing implicit-explicit Runge–Kutta methods for gradient flows, *Mathematics of Computation* 93 (350) (2024) 2745–2767. doi:10.1090/mcom/3950.

- [8] W. Cao, H. Yang, W. Chen, An Exponential Time Differencing Runge–Kutta Method ETDRK32 for Phase Field Models, *Journal of Scientific Computing* 99 (1) (2024) 6. doi:10.1007/s10915-024-02474-9.
- [9] Z.-q. K. Tian, D. Zhou, Exponential Time Differencing Algorithm for Pulse-Coupled Hodgkin-Huxley Neural Networks, *Frontiers in Computational Neuroscience* 14 (2020) 40. doi:10.3389/fncom.2020.00040.
- [10] Z. Fu, J. Yang, Energy-decreasing exponential time differencing Runge–Kutta methods for phase-field models, *Journal of Computational Physics* 454 (2022) 110943. doi:10.1016/j.jcp.2022.110943.
- [11] X. Wang, L. Ju, Q. Du, Efficient and stable exponential time differencing Runge–Kutta methods for phase field elastic bending energy models, *Journal of Computational Physics* 316 (2016) 21–38. doi:10.1016/j.jcp.2016.04.004.
- [12] Z. Fu, J. Shen, J. Yang, Higher-order energy-decreasing exponential time differencing Runge-Kutta methods for gradient flows, *Science China Mathematics* (2024) 1–20doi:10.1007/s11425-024-2337-3.
- [13] M. Raissi, P. Perdikaris, G. E. Karniadakis, Physics-informed neural networks: A deep learning framework for solving forward and inverse problems involving nonlinear partial differential equations, *Journal of Computational Physics* 378 (2019) 686–707. doi:10.1016/j.jcp.2018.10.045.
- [14] J. Sirignano, K. Spiliopoulos, DGM: A deep learning algorithm for solving partial differential equations, *Journal of Computational Physics* 375 (2018) 1339–1364. doi:10.1016/j.jcp.2018.08.029.
- [15] Y. Zang, G. Bao, X. Ye, H. Zhou, Weak adversarial networks for high-dimensional partial differential equations, *Journal of Computational Physics* 411 (2020) 109409. doi:10.1016/j.jcp.2020.109409.
- [16] W. E, B. Yu, The deep Ritz method: A deep learning-based numerical algorithm for solving variational problems, *Communications in Mathematics and Statistics* 6 (1) (2018) 1–12. doi:10.1007/s40304-018-0127-z.

- [17] L. Lu, P. Jin, G. Pang, Z. Zhang, G. E. Karniadakis, Learning nonlinear operators via DeepONet based on the universal approximation theorem of operators, *Nature Machine Intelligence* 3 (3) (2021) 218–229. doi:10.1038/s42256-021-00302-5.
- [18] J. Han, A. Jentzen, W. E, Solving high-dimensional partial differential equations using deep learning, *Proceedings of the National Academy of Sciences* 115 (34) (2018) 8505–8510. doi:10.1073/pnas.1718942115.
- [19] W. Xiong, X. Long, S. P. Bordas, C. Jiang, The deep finite element method: A deep learning framework integrating the physics-informed neural networks with the finite element method, *Computer Methods in Applied Mechanics and Engineering* 436 (2025) 117681. doi:10.1016/j.cma.2024.117681.
- [20] G. Grekas, C. G. Makridakis, Deep Ritz - Finite element methods: Neural network methods trained with finite elements, *Computer Methods in Applied Mechanics and Engineering* 437 (2025) 117798. doi:10.1016/j.cma.2025.117798.
- [21] J. Bruna, B. Peherstorfer, E. Vanden-Eijnden, Neural Galerkin Scheme with Active Learning for High-Dimensional Evolution Equations (May 2022). arXiv:2203.01360.
- [22] Z. Liu, W. Cai, Z.-Q. John Xu, Multi-Scale Deep Neural Network (MscaleDNN) for Solving Poisson-Boltzmann Equation in Complex Domains, *Communications in Computational Physics* 28 (5) (2020) 1970–2001. doi:10.4208/cicp.0A-2020-0179.
- [23] J. Yang, Q. Zhu, A Local Deep Learning Method for Solving High Order Partial Differential Equations, *Numerical Mathematics: Theory, Methods and Applications* 15 (1) (2022) 42–67. doi:10.4208/nmtma.0A-2021-0035.
- [24] C. L. Wight, J. Zhao, Solving Allen-Cahn and Cahn-Hilliard Equations Using the Adaptive Physics Informed Neural Networks, *Communications in Computational Physics* 29 (3) (2021) 930–954. doi:10.4208/cicp.0A-2020-0086.

- [25] Z. Wang, Z. Zhang, A mesh-free method for interface problems using the deep learning approach, *Journal of Computational Physics* 400 (2020) 108963. doi:10.1016/j.jcp.2019.108963.
- [26] M. Kütük, H. Yücel, Energy dissipation preserving physics informed neural network for Allen–Cahn equations, *Journal of Computational Science* (2025) 102577doi:10.1016/j.jocs.2025.102577.
- [27] Z. Hu, C. Liu, Y. Wang, Z. Xu, Energetic Variational Neural Network Discretizations of Gradient Flows, *SIAM Journal on Scientific Computing* 46 (4) (2024) A2528–A2556. doi:10.1137/22M1529427.
- [28] J. Zhang, S. Zhang, J. Shen, G. Lin, Energy-dissipative evolutionary deep operator neural networks, *Journal of Computational Physics* 498 (2024) 112638. doi:10.1016/j.jcp.2023.112638.
- [29] J. Yang, Y. Zhao, Q. Zhu, ε -rank and the Staircase Phenomenon: New Insights into Neural Network Training Dynamics (2025). arXiv:2412.05144.
- [30] G.-B. Huang, L. Chen, C.-K. Siew, Universal Approximation using Incremental Constructive Feedforward Networks with Random Hidden Nodes, *IEEE Transactions on Neural Networks* 17 (4) (2006) 879–892. doi:10.1109/TNN.2006.875977.
- [31] A. Rahimi, B. Recht, Random Features for Large-Scale Kernel Machines, *Advances in neural information processing systems* 20 (2007).
- [32] J. Chen, W. E, Y. Luo, The Random Feature Method for Time-Dependent Problems, *East Asian Journal on Applied Mathematics* 13 (3) (2023) 435–463. doi:10.4208/eajam.2023-065.050423.
- [33] N. H. Nelsen, A. M. Stuart, The Random Feature Model for Input-Output Maps between Banach Spaces, *SIAM Journal on Scientific Computing* 43 (5) (2021) A3212–A3243. doi:10.1137/20M133957X.
- [34] S. Dong, Z. Li, Local extreme learning machines and domain decomposition for solving linear and nonlinear partial differential equations, *Computer Methods in Applied Mechanics and Engineering* 387 (2021) 114129. doi:10.1016/j.cma.2021.114129.

- [35] J. Chen, W. E, Y. Sun, Optimization of Random Feature Method in the High-Precision Regime, *Communications on Applied Mathematics and Computation* 6 (2) (2024) 1490–1517. doi:10.1007/s42967-024-00389-8.
- [36] T. Tang, J. Yang, Y. Zhao, Q. Zhu, Structured First-Layer Initialization Pre-Training Techniques to Accelerate Training Process Based on ε -Rank (2025). arXiv:2507.11962.
- [37] A.-K. Kassam, L. N. Trefethen, Fourth-Order Time-Stepping for Stiff PDEs, *SIAM Journal on Scientific Computing* 26 (4) (2005) 1214–1233. doi:10.1137/S1064827502410633.
- [38] C. A. Kennedy, M. H. Carpenter, Diagonally implicit Runge–Kutta methods for stiff ODEs, *Applied Numerical Mathematics* 146 (2019) 221–244. doi:10.1016/j.apnum.2019.07.008.
- [39] S. M. Allen, J. W. Cahn, A microscopic theory for antiphase boundary motion and its application to antiphase domain coarsening, *Acta Metallurgica* 27 (6) (1979) 1085–1095. doi:10.1016/0001-6160(79)90196-2.
- [40] J. Shen, X. Yang, Numerical approximations of Allen-Cahn and Cahn-Hilliard equations, *Discrete & Continuous Dynamical Systems* 28 (4) (2010) 1669–1691. doi:10.3934/dcds.2010.28.1669.
- [41] J. W. Cahn, J. E. Hilliard, Free Energy of a Nonuniform System. I. Interfacial Free Energy, *The Journal of Chemical Physics* 28 (2) (1958) 258–267. doi:10.1063/1.1744102.